MOX–Report No. 44/2012

A numerical method for two-phase flow in fractured porous media with non-matching grids

Fumagalli, A.; Scotti, A.

MOX, Dipartimento di Matematica "F. Brioschi"
Politecnico di Milano, Via Bonardi 9 - 20133 Milano (Italy)

mox@mate.polimi.it http://mox.polimi.it

A numerical method for two-phase flow in fractured porous media with non-matching grids

Alessio Fumagalli[♯] and Anna Scotti[♯]

September 27, 2012

[♯] MOX– Modellistica e Calcolo Scientifico
Dipartimento di Matematica "F. Brioschi"
Politecnico di Milano
via Bonardi 9, 20133 Milano, Italy
alessio.fumagalli@mail.polimi.it
anna.scotti@mail.polimi.it

Keywords: Two-phase flow, reduced models, fractured porous media, XFEM.

AMS Subject Classification: 05A16, 65N38, 78M50

Abstract

We propose a novel computational method for the efficient simulation of two-phase flow in fractured porous media. Instead of refining the grid to capture the flow along the faults or fractures, we represent them as immersed interfaces with a reduced model for the flow and suitable coupling conditions. We allow for non matching grids between the porous matrix and the fractures to increase the flexibility of the method in realistic cases. We employ the extended finite element method for the Darcy problem and a finite volume method that is able to handle cut cells and matrix-fracture interactions for the saturation equation. The choice of a suitable flux function in the case of discontinuous flux function at the interface between the fracture and the porous matrix is also addressed through numerical experiments.

1 Introduction

It has been observed that fractures and faults in porous media can act as conduits or barriers for the flow. A relevant application that requires an accurate characterization of the faults from the geo-mechanical and hydrodynamic point of view is the study of CO_2 injection and storage, see [16]. At injection conditions, CO_2 is buoyant relative to the ambient groundwater, so it rises toward

the top of the formation and, in the presence of a pre-existing well or fracture, or the activation of a fault, can leak into shallower formations.
The effect of fractures on the flow is important in many different applications such as the study of fractured aquifers, geothermal fields, oil and gas reservoirs and unconventional hydrocarbon sources.
In all the aforementioned applications the presence of large fractures or faults influences the flow in a complex way that cannot be reproduced in numerical simulations by simple homogenization. The space scale of these features is usually such that a very fine mesh is needed, leading to an extremely high computational cost. The typical width of fractures (of the order of centimetres) and faults (of the orders of meters) is indeed very small compared to the size of the domain of interest that ranges from hundreds on meters for reservoir scale simulations to hundreds of kilometres at basin scale.
One possibility to address this problem is to use a reduced model to represent the flow in fractures, represented as immersed interfaces coupled with the rest of the porous medium. This approach was first introduced by Alboin *et al.*, [2] for single-phase Darcy problems in porous media in the presence of permeable fractures, and later extended by Martin *et al.*, [17] and Angot, [3] to more general coupling conditions and geometric configurations. In [7] this approach is further extended to allow for non-matching grids between the porous medium and the fracture thanks to the use of the extended finite element method (XFEM). Removing the constraint of mesh conformity can be convenient in realistic cases with numerous and complex fractures. An advantage of a non-matching method is the possibility to run multiple simulations with different fractures configuration, in the case of uncertainty on geophysical parameters or multiple scenario analyses, without meshing the domain each time.
In this paper we present an original numerical approximation strategy for two-phase flow in fractured media. We complement the generalized Darcy problem, approximated as in [7], with an evolution equation for the saturation of one of the two phases, to obtain a fractional flow formulation of the two-phase Darcy problem. A solution strategy for the two-phase flow in fractured porous media in the framework of reduced models was first introduced in [13]. In this work we consider the case of negligible capillary effects and set up for the resulting hyperbolic problem a discretization scheme that can handle non matching grids. In particular, the finite volume scheme should deal with cut cells and account for the interactions between the porous matrix and the fracture. As concerns the time discretization an explicit scheme is considered and the coupling between the Darcy problem and the saturation equation is solved via an Implicit Pressure - Explicit Saturation (IMPES) splitting. The faults and the surrounding porous matrix can be regarded as two different rock types characterized by different values of the absolute permeability tensor. In general, they might also be assigned different relative permeability functions. As a result the saturation equation has a flux function that is discontinuous at the matrix-fracture interface. In this type of problems the choice of the numerical flux is crucial to obtain an accurate

solution. It was shows [18] that in some cases an approximate solution of the Riemann problem at the interface could lead not only to inaccurate solutions but, more important, yield unphysical solutions that do not satisfy the entropy condition. In this work we will employ the upstream mobility flux for the solution of some relevant test cases and compare the results with those obtained with an exact Riemann solver to identify possible limits of the approximate solvers for the problem of our interest. The paper is organized as follows. In Section 2 the governing equations for the two-phase flow are presented. The reduced model for the flow in the fracture and the interface conditions that couple the bulk and the fracture are discussed in Section 3. The numerical discretization of the problem is presented in Section 4. Section 5 is devoted to some synthetic test cases with the aim of verifying the properties of the method and assessing its effectiveness.

2 Governing equations

We consider two immiscible fluid phases, denoted by the subscript $\alpha \in \{w, n\}$ for the wetting and non-wetting phase respectively, flowing in a porous medium crossed by fractures. The latter can be characterized by data, *e.g.* permeabilities, that differ significantly from the porous matrix. We neglect the effect of capillary pressure.
Let us consider a regular domain $\Omega \in \mathbb{R}^n$, $n = 2$ or 3, with boundary $\overline{\Gamma} = \overline{\Gamma}_N \cup \overline{\Gamma}_D$, $\Gamma_N \neq \emptyset$, and outward unit normal $\boldsymbol{n}_\Gamma$, cut by a thin region $\Omega_f \subset \Omega$ of thickness d representing the fracture. Let us set, from now on, $i \in \{1, 2, f\}$. Figure 1 represents the partition $\overline{\Omega} = \bigcup_i \overline{\Omega}_i$ into three disjoint subsets of Ω. The

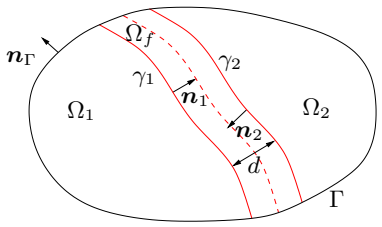

Figure 1: Sketch of Ω with Ω_1 and Ω_2 divided by Ω_f.

interfaces between Ω_j, with $j \in \{1, 2\}$, and Ω_f are denoted as $\gamma_j \in \mathbb{R}^{n-1}$ and have unit normal $\boldsymbol{n}_j$, pointing outwards with respect to Ω_j. If we introduce the interval of time $\mathcal{I}_T := (0, T)$ the space-time domains are defined as $Q_i := \Omega_i \times \mathcal{I}_T$. The equations that describe the two-phase flow can be written in the so called *fractional flow formulation* [6, 13], as a system formed by a generalized Darcy problem and the saturation equation. The unknowns are the total velocity $\boldsymbol{u}$ defined as the sum of the two phase velocities, the global pressure p, an artificial variable related to the phase pressures, see [6], and the saturation of the non-wetting phase, from now on denoted as S, with $S \in [0, 1]$. The system reads

$$\begin{cases} \nabla\cdot \boldsymbol{u}_i = 0 \\ \boldsymbol{u}_i = -\lambda_i \boldsymbol{K}_i \left(\nabla p_i - \boldsymbol{G}_i\right) \\ \Phi_i \dfrac{\partial S_i}{\partial t} + \nabla\cdot \boldsymbol{v}_i = 0 \\ \boldsymbol{v}_i = f_i \boldsymbol{u}_i + b_i \boldsymbol{K}_i \boldsymbol{g} \end{cases} \qquad \text{in } Q_i, \tag{1a}$$

coupled with

$$\begin{cases} \boldsymbol{u}_j \cdot \boldsymbol{n}_j = \boldsymbol{u}_f \cdot \boldsymbol{n}_j \\ p_j = p_f \\ \boldsymbol{v}_j \cdot \boldsymbol{n}_j = \boldsymbol{v}_f \cdot \boldsymbol{n}_j \end{cases} \qquad \text{on } \gamma_j \times \mathcal{I}_T, \tag{1b}$$

where the subscripts i and j denotes the restriction of the variables to Q_i or γ_j, respectively. Furthermore we have set

$$\lambda_i := \frac{k_i^n}{\mu^n} + \frac{k_i^w}{\mu^w}, \quad \boldsymbol{G}_i := \frac{k_i^w \rho^w/\mu^w + k_i^n \rho^n/\mu^n}{\lambda_i}\boldsymbol{g},$$
$$f_i := \frac{k_i^n}{\mu^n \lambda_i}, \qquad b_i := \frac{k_i^n k_i^w}{\mu^n \mu^w \lambda_i}\left(\rho^n - \rho^w\right).$$

Here $\boldsymbol{K}_i$ denotes the absolute permeability tensor which is symmetric and positive definite and Φ_i is the porosity. It is important to note that in realistic situations the entries of $\boldsymbol{K}_i$ can differ of several orders of magnitude from the neighbouring subdomains. For each phase α, k^α is the relative permeability, ρ^α the density and μ^α the dynamic viscosity. Finally $\boldsymbol{g}$ is the gravity acceleration vector. The relative permeabilities are non-linear functions of the saturation [4] and in principle different shapes could be associated with different rock types.
Usually, the first two equations of (1) are called *pressure equations*, while the last two are called *saturation equations*.
Let us introduce a discretization of the time interval, dividing $\mathcal{I}_T$ into N subintervals

$$\mathcal{I}_T^m := \left(t^m, t^{m+1}\right) \quad \text{with} \quad \Delta t^m := \left|\mathcal{I}_T^m\right|,$$

such that $\overline{\mathcal{I}_T} = \bigcup_m \overline{\mathcal{I}_T^m}$ for $m \in \{0, \ldots, N\}$. Using an *IMPES* type approach [6] to solve (1) we decouple the pressure equations from the saturation equations, and we solve them in sequence at each time step $\mathcal{I}_T^m$. Hence the pressure equations, with fixed saturation $S^{(m)}$ at $\mathcal{I}_T^m$, read

$$\begin{cases} \nabla \cdot \boldsymbol{u}_i = 0 \\ \boldsymbol{u}_i = -\lambda_i(S^{(m)}) \boldsymbol{K}_i \left[\nabla p_i - \boldsymbol{G}_i(S^{(m)})\right] \end{cases} \qquad \text{in } \Omega_i \times \mathcal{I}_T^{m+1}, \tag{2a}$$

with the following coupling conditions

$$\begin{cases} \boldsymbol{u}_j \cdot \boldsymbol{n}_j = \boldsymbol{u}_f \cdot \boldsymbol{n}_j \\ p_j = p_f \end{cases} \qquad \text{on } \gamma_j \times \mathcal{I}_T^{m+1}. \tag{2b}$$

We impose to (2) the following boundary conditions

$$\begin{cases} p_i = \overline{p}_i & \text{on } \Gamma_N \\ \boldsymbol{u}_i \cdot \boldsymbol{n}_\Gamma = \overline{u}_i & \text{on } \Gamma_D \end{cases}$$

Once the pressure equations have been solved the saturation equations, with the computed total velocity $\boldsymbol{u}_i^{(m+1)}$ at time $\mathcal{I}_T^{m+1}$, read

$$\begin{cases} \Phi_i \dfrac{\partial S_i}{\partial t} + \nabla \cdot \boldsymbol{v}_i = 0 \\ \boldsymbol{v}_i = f_i \boldsymbol{u}_i^{(m+1)} + b_i \boldsymbol{K}_i \boldsymbol{g} \end{cases} \quad \text{in } \Omega_i \times \mathcal{I}_T^{m+1}, \tag{3a}$$

with the coupling conditions

$$\boldsymbol{v}_j \cdot \boldsymbol{n}_j = \boldsymbol{v}_f \cdot \boldsymbol{n}_j \quad \text{on } \gamma_j \times \mathcal{I}_T^{m+1}. \tag{3b}$$

We impose to (3) the following boundary and initial conditions

$$\begin{cases} S_i = \overline{S}_i & \text{on } \Gamma_N \\ \boldsymbol{v}_i \cdot \boldsymbol{n}_\Gamma = \overline{v}_i & \text{on } \Gamma_D \end{cases} \quad \text{and} \quad S_i = S_i^0 \quad \text{in } \Omega_i \times \{0\}$$

Note that the coupling conditions at the interface between two different rock types prescribe the continuity of the normal component of the phase velocity, *i.e.* the normal flux. In the case of discontinuous flux function this condition does not imply the continuity of saturation which will be, in general, discontinuous at the interface.

3 Reduced model for the two-phase flow

Following [13, 10], we want to employ a reduced model for problems (2) and (3) in the fractures, replacing the region Ω_f with a $n-1$ dimensional interface $\gamma \approx \gamma_j$ with unit normal $\boldsymbol{n} \approx \boldsymbol{n}_1 \approx -\boldsymbol{n}_2$, as shown in Figure 2 for $n = 2$.

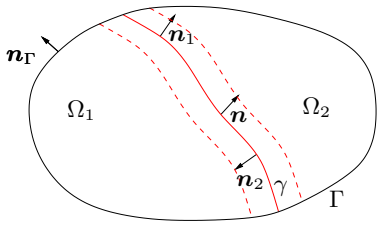

Figure 2: Sketch of Ω cut by the interface γ that replaces Ω_f.

If the pressure and saturation equations are decoupled with a sequential splitting as shown in the previous section it can be observed that the generalized Darcy problem for the global pressure and total velocity has the same structure as the single phase Darcy problem. Thus, a reduced model can be derived as in [17].

We report the main results for readers convenience. Given a scalar or vector function $a : \Omega \to \mathbb{R}^q$, $q = 1$ or n, let us define

$$[\![a]\!]_\gamma := a_1 - a_2 \quad \text{and} \quad \{\{a\}\}_\gamma := \frac{a_1 + a_2}{2}$$

where we have indicated with

$$a_j(\boldsymbol{x}) := \lim_{\epsilon \to 0^\pm} a(\boldsymbol{x} - \epsilon \boldsymbol{n}) \quad \text{and} \quad \boldsymbol{x} \in \gamma.$$

We introduce the projection matrices $\boldsymbol{N} := \boldsymbol{n} \otimes \boldsymbol{n}$ and $\boldsymbol{T} := \boldsymbol{I} - \boldsymbol{N}$ so that, given $e : \Omega \to \mathbb{R}$ and $\boldsymbol{c} : \Omega \to \mathbb{R}^n$ the tangential gradient and tangential divergence are

$$\nabla_{\boldsymbol{\tau}} e := \boldsymbol{T} \nabla e \quad \text{and} \quad \nabla_{\boldsymbol{\tau}} \cdot \boldsymbol{c} := \boldsymbol{T} : \nabla \boldsymbol{c}.$$

From now on we will indicate with $\hat{\cdot}$ the reduced variables defined on γ. The scalar unknowns $\hat{p}$ and $\hat{S}$ represent the averaged values across normal sections of Ω_f, given $\boldsymbol{s} \in \gamma$ we have

$$\hat{h}(\boldsymbol{s}) := \frac{1}{d} \int_{-\frac{d}{2}}^{\frac{d}{2}} h_f(\boldsymbol{s} + r\boldsymbol{n})\, dr \quad \text{for } h = p,\, S.$$

The vector unknowns $\hat{\boldsymbol{u}}$ and $\hat{\boldsymbol{v}}$ are the tangential fluxes integrated over the normal sections of Ω_f, namely

$$\hat{\boldsymbol{m}}(\boldsymbol{s}) := \int_{-\frac{d}{2}}^{\frac{d}{2}} \boldsymbol{T} \boldsymbol{m}_f(\boldsymbol{s} + r\boldsymbol{n})\, dr \quad \text{for } \boldsymbol{m} = \hat{\boldsymbol{u}},\, \hat{\boldsymbol{v}}. \tag{4}$$

The properties of the fracture are averaged over each cross sections of Ω_f or assumed to be invariant in the normal direction. We assume that $\boldsymbol{K}_f = K_{f,\boldsymbol{n}} \boldsymbol{N} + K_{f,\boldsymbol{\tau}} \boldsymbol{T}$, with $K_{f,\boldsymbol{n}}$ and $K_{f,\boldsymbol{\tau}}$ bounded and strictly positive. Equation (2) can be written as

$$\begin{cases} \nabla \cdot \boldsymbol{u}_j = 0 \\ \boldsymbol{u}_j = -\lambda_j \boldsymbol{K}_j (\nabla p_j - \boldsymbol{G}_j) \end{cases} \quad \text{in } \Omega_j \times \mathcal{I}_T^{m+1}, \tag{5a}$$

coupled with

$$\begin{cases} \nabla_{\boldsymbol{\tau}} \cdot \hat{\boldsymbol{u}} = [\![\boldsymbol{u} \cdot \boldsymbol{n}]\!]_\gamma \\ \hat{\eta} \hat{\boldsymbol{u}} + \nabla_{\boldsymbol{\tau}} \hat{p} = \hat{\boldsymbol{G}} \end{cases} \quad \text{in } \gamma \times \mathcal{I}_T^{m+1}, \tag{5b}$$

where $\hat{\boldsymbol{G}}$ is the tangential component of $\boldsymbol{G}$ integrated over each normal section of Ω_f, as in (4), and we have set $\hat{\eta} := d/(\lambda_f K_{f,\boldsymbol{\tau}})$,. Introducing a shape parameter $\xi_0 \in (0, 0.25]$, for model closure, see [17, 3, 8], and setting $\eta_\gamma^{-1} := d\lambda_f K_{f,\boldsymbol{n}}$, the coupling conditions can be written as

$$\begin{cases} \xi_0 \eta_\gamma [\![\boldsymbol{u} \cdot \boldsymbol{n}]\!]_\gamma + \dfrac{d}{4} [\![\boldsymbol{G} \cdot \boldsymbol{n}]\!]_\gamma = \{\{p\}\}_\gamma - \hat{p} \\ \eta_\gamma \{\{\boldsymbol{u} \cdot \boldsymbol{n}\}\}_\gamma = [\![p]\!]_\gamma + d\{\{\boldsymbol{G} \cdot \boldsymbol{n}\}\}_\gamma \end{cases} \quad \text{on } \gamma \times \mathcal{I}_T^{m+1}.$$

Similarly to (2) the reduced equations for (3) become

$$\begin{cases} \Phi_j \dfrac{\partial S_j}{\partial t} + \nabla \cdot \boldsymbol{v}_j = 0 \\ \boldsymbol{v}_j = f_j \boldsymbol{u}_j + b_j \boldsymbol{K}_j \boldsymbol{g} \end{cases} \qquad \text{in } \Omega_j \times \mathcal{I}_T^{m+1}, \tag{6a}$$

coupled with

$$\begin{cases} d\Phi_f \dfrac{\partial \hat{S}}{\partial t} + \nabla_{\boldsymbol{\tau}} \cdot \hat{\boldsymbol{v}} = [\![\boldsymbol{v} \cdot \boldsymbol{n}]\!]_\gamma \\ \hat{\boldsymbol{v}} = f_f \hat{\boldsymbol{u}} + b_f K_{f,\boldsymbol{\tau}} \hat{\boldsymbol{g}} \end{cases} \qquad \text{in } \gamma \times \mathcal{I}_T^{m+1}, \tag{6b}$$

where $\hat{\boldsymbol{g}}$ is the tangential component of $\boldsymbol{g}$ integrated over each normal section of Ω_f, as in (4). The coupling conditions between Ω_j now read

$$\boldsymbol{v}_j(S_j) \cdot \boldsymbol{n}_j = \boldsymbol{v}_{f,j}(\hat{S}) \cdot \boldsymbol{n}_j \quad \text{on } \gamma, \tag{7}$$

with

$$\boldsymbol{v}_{f,j}(\hat{S}) := f_f(\hat{S}) \boldsymbol{u}_j + b_f(\hat{S}) K_{f,\boldsymbol{n}} \boldsymbol{N} \boldsymbol{g}.$$

4 Numerical approximation of the two-phase Darcy problem

The Darcy problem (2) is solved in mixed form, with the lowest order Raviart-Thomas finite elements enriched in the cut elements by means of the XFEM. The finite element spaces for velocity and pressure are constructed as proposed in [12], replicating the degrees of freedom in the cut elements and restricting the corresponding basis functions to each of the subdomains Ω_i, see [7, 9]. The choice of mixed finite elements guarantees a locally conservative velocity field for the subsequent solution of the saturation equation (3), which is carried out with the finite volumes method in the porous medium and in the fracture. We employ the same computational grids for the discretization of the Darcy problem and the saturation equations. Therefore, the finite volume solver for the porous medium has to allow for cut elements. Moreover, additional terms will account for matrix-fracture exchanges due to the coupling conditions (7).

Let $\mathcal{T}_h$ be the triangulation of the domain Ω. We define $\mathcal{U}_h \subset \mathcal{T}_h$ as the set of element that are not cut by the fracture, and $\mathcal{C}_h \subset \mathcal{T}_h$ as the set of cut elements, thus $\mathcal{T}_h = \mathcal{U}_h \cup \mathcal{C}_h$. If $K \in \mathcal{C}_h$, we denote as K_j, each of the sub-elements generated by the cut of the fracture, *i.e.* $K_j := K \cap \Omega_j$, as Figure 3 shows.

Moreover, let $\hat{\mathcal{T}}_h$ be the mesh of the fracture γ.

We can now define the spaces for the approximation of the saturation S_h in Ω and of $\hat{S}_h$ in γ. As concerns S_h, similarly to what is done to approximate pressure in [7, 9], we consider the discrete saturation as made of two components, associated to the domains Ω_j. The solution is then sought in $Q_h := Q_{1,h} \times Q_{2,h}$, with

$$Q_{j,h} := \left\{ q_h \in L^2(\Omega_j) \ : \ q_{h|_{K_j}} \in \mathbb{P}_0(K_j) \ \forall K \in \mathcal{T}_h \right\},$$

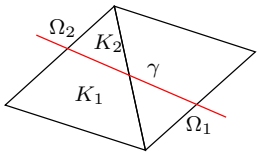

Figure 3: Sketch of an element $K = K_1 \cup K_2$ cut by γ.

where, for any $K \in \mathcal{T}_h$,

$$\mathbb{P}_0(K \cap \Omega_j) = \left\{ q_{h|_{K_j}} : q_h \in \mathbb{P}_0(K) \right\}$$

is the linear space of the restrictions to K_j of the standard piecewise constant local functions. The discrete saturation can thus be discontinuous across γ as required by the coupling conditions (7) in the case of a discontinuous flux function, being defined on each part of a cut element $K \in \mathcal{C}_h$ by independent $\mathbb{P}_0$ local functions.
The approximate solution $\hat{S}_h$ for the saturation in the fracture is sought in the following space

$$\hat{Q}_h := \left\{ \hat{q} \in L^2(\gamma) : \ \hat{q}|_{\hat{K}} \in \mathbb{P}_0\left(\hat{K}\right), \ \hat{K} \in \hat{\mathcal{T}}_h \right\}.$$

In the case of uncut elements, *i.e.* for $K \in \mathcal{U}_h$, the explicit finite volume approximation of (6) reads

$$\int_K \phi \frac{S_h^{m+1} - S_h^m}{\Delta t^m} d\boldsymbol{x} + \int_{\partial K} \boldsymbol{F}(S_h^m) \cdot \boldsymbol{n}_K ds = 0$$

where $\boldsymbol{F}$ is a suitable numerical flux and $\boldsymbol{n}_K$ is the outward unit normal to ∂K. In the cut elements the method has to be modified to account for the cut edges and for the presence of the fracture. Each sub-element K_j indeed, as shown in Figure 4, shares edges with the neighbouring elements in $\mathcal{U}_h$, or sub-elements contained in $\mathcal{C}_h$. Moreover, one of the edges of each K_j is formed by the elements, segments for $n = 2$ or triangles for $n = 3$, of $\hat{\mathcal{T}}_h$.
Thus, for all $K \in \mathcal{C}_h$ we have

$$\begin{aligned} \int_{K \cap \Omega_j} \phi \frac{S_h^{m+1} - S_h^m}{\Delta t^m} d\boldsymbol{x} + \int_{\partial K \cap \Omega_j} \boldsymbol{F}(S_h^m) \cdot \boldsymbol{n}_K ds + \\ + \int_{\gamma \cap K} (-1)^{j+1} \boldsymbol{F}\left(S_h^m, \mathcal{M}(\hat{S}_h^m)\right) \cdot \boldsymbol{n} \, ds = 0, \end{aligned}$$

where $\mathcal{M}(\hat{S}_h^m)$ is the interpolation of $\hat{S}_h^m$ on $\mathcal{T}_h$, *i.e.* we have $\mathcal{M} : \hat{Q}_h \to Q_h$. The two meshes are indeed, in general, *genuinely* non matching as shown in Figure 4. Conversely, the mass balance for each element of $\hat{\mathcal{T}}_h$ has to account for the

flux due to one or more elements of $\mathcal{C}_h$. The discrete problem in the fracture can be written, for every $\hat{K} \in \hat{\mathcal{T}}_h$, as

$$\int_{\hat{K}} d\phi_f \frac{\hat{S}_h^{m+1} - \hat{S}_h^m}{\Delta t^m} dx + \int_{\partial \hat{K}} \hat{\boldsymbol{F}}(\hat{S}_h^m) \cdot \boldsymbol{n}_{\hat{K}} ds +$$
$$- \sum_{j=1,2} \int_{\gamma \cap K} (-1)^{j+1} \mathcal{M}^* \left(\hat{\boldsymbol{F}} \left(S_h^m, \mathcal{M}(\hat{S}_h^m) \right) \cdot \boldsymbol{n} \right) ds = 0.$$

Here the operator $\mathcal{M}^* : Q_h \to \hat{Q}_h$ performs the interpolation of the saturation from $\mathcal{T}_h$ to $\hat{\mathcal{T}}_h$, which is the adjoint operator of $\mathcal{M}$. We represent the operators $\mathcal{M}$ and $\mathcal{M}^*$ with a matrix $\boldsymbol{M}$ and its transpose respectively, its entries are given by

$$\boldsymbol{M}_{ij} = \int_{\hat{K}_j \cap K_i} 1 d\boldsymbol{x} \tag{8}$$

where the subscript i, j denote the i-th element of $\mathcal{T}_h$ and the j-th element of $\hat{\mathcal{T}}_h$. The integral in (8) is approximated with a Gaussian quadrature formula. The

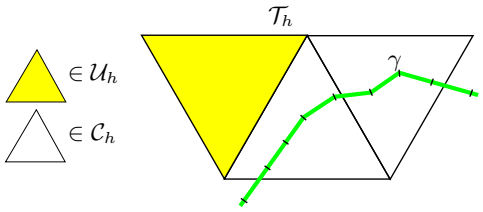

Figure 4: Sketch of $\mathcal{T}_h$ cut by γ. The mesh of γ is in general non-matching with the edges of the cut elements.

choice of the numerical flux is critical in problems characterized, like the one of our interest, by a discontinuous flux function due to the presence of different rock types, typically the matrix and the fracture. For two-phase flow in porous media a numerical flux that is commonly used, in particular by petroleum engineers, is the upstream mobility (UM) flux citeBrenier1991, which can be considered as an approximate solution to the Riemann problems at the interfaces, based on simple physical considerations. The upstream mobility flux $\boldsymbol{F}^{UM}$, for both the medium and the fracture, is given by

$$\boldsymbol{F}^{UM}(\alpha, \beta) = f^* \boldsymbol{u} + b^* \boldsymbol{K} \boldsymbol{g}$$

where

$$f^* = \begin{cases} f(\alpha) & \text{if } \boldsymbol{v} \cdot \boldsymbol{n} > 0 \\ f(\beta) & \text{if } \boldsymbol{v} \cdot \boldsymbol{n} \leq 0 \end{cases}, \quad b^* = \begin{cases} b(\alpha) & \text{if } \boldsymbol{v} \cdot \boldsymbol{n} > 0 \\ b(\beta) & \text{if } \boldsymbol{v} \cdot \boldsymbol{n} \leq 0 \end{cases}.$$

At the interface between two different rock types the above definition must be adapted, as in [18]. Let us denote with $\boldsymbol{v}_-$ and $\boldsymbol{v}_+$ the flux functions on the opposite sides of the interface. The same subscript denote the values of f and b. Moreover, we indicate with α and β the values of saturation on the two sides of the discontinuity. The interface flux $\overline{\boldsymbol{F}}^{UM}(\alpha, \beta)$ is computed choosing

$$f^* = \begin{cases} f_-(\alpha) & \text{if } \boldsymbol{v} \cdot \boldsymbol{n} > 0 \\ f_+(\beta) & \text{if } \boldsymbol{v} \cdot \boldsymbol{n} \leq 0 \end{cases}, \; b^* = \begin{cases} b_-(\alpha) & \text{if } \boldsymbol{v} \cdot \boldsymbol{n} > 0 \\ b_+(\beta) & \text{if } \boldsymbol{v} \cdot \boldsymbol{n} \leq 0 \end{cases},$$

and is such that, for some saturation $\overline{S}$,

$$\overline{\boldsymbol{F}}^{UM}(\alpha, \overline{S}) = \boldsymbol{F}_-^{UM}(\alpha, \overline{S}) = \boldsymbol{F}_+^{UM}(\overline{S}, \beta).$$

An alternative choice for the numerical flux is the Godunov flux [11], which corresponds to solving exactly the Riemann problems at the element interfaces, hence we indicate it as ERS. At the interface between two rock types the Godunov flux must be redefined to account for the discontinuous flux function. In [5] the Godunov flux at the interface is defined as the unique solution $\overline{\boldsymbol{F}}^{ERS}(\alpha, \beta)$ satisfying

$$\overline{\boldsymbol{F}}^{ERS}(\alpha, \beta) = \boldsymbol{F}_-^{ERS}(\alpha, \overline{S}) = \boldsymbol{F}_+^{ERS}(\overline{S}, \beta)$$

for some $\overline{S}$. Recipes for the computation of $\boldsymbol{F}^{ERS}$ are discussed in [14], and can be summarized in the following single, easy to implement, expression [18]

$$\overline{\boldsymbol{F}}^{ERS}(\alpha, \beta) = \min\left\{\boldsymbol{v}_-(\min(\alpha, \theta_-)), \boldsymbol{v}_+(\max(\beta, \theta_+))\right\}.$$

Here, we have assumed that $\boldsymbol{v}_-$ and $\boldsymbol{v}_+$ have only one local maximum point, denoted by θ_- and θ_+ respectively. A similar expression can be derived in the case of one local minimum. In the next sections we will consider both choices for the numerical flux applied to some significant test case to investigate possible advantages or shortcomings of both numerical fluxes.

5 Test Cases

In this section we present some test cases with the aim of validating the proposed method and assessing it properties and possible advantages and limits.

5.1 Numerical validation

Let us consider a rectangular domain $\Omega = (0, 1) \times (-4, 4)$ occupied by two different rock types, denoted with the subscripts $\pm$, for $y > 0$ and $y < 0$ respectively. The two types of rock are characterized by different isotropic absolute permeabilities $K_\pm$, *i.e.* $\boldsymbol{K} = K_\pm \boldsymbol{I}$, while the relative permeability is the same and

linear with saturation. We set $K_+ = 2$, $K_- = 1$, while $k^w = S$ and $k^n = 1 - S$ everywhere. Moreover we have

$$\rho^w |\boldsymbol{g}| = 2, \quad \rho^n |\boldsymbol{g}| = 1, \quad \mu^w = \mu^n = 1,$$
$$\boldsymbol{u} = \boldsymbol{0} \quad \text{and} \quad \Phi = 1.$$

The flux function is thus discontinuous at $y = 0$: the shape of $\boldsymbol{v}_\pm$ is reported in Figure 5.

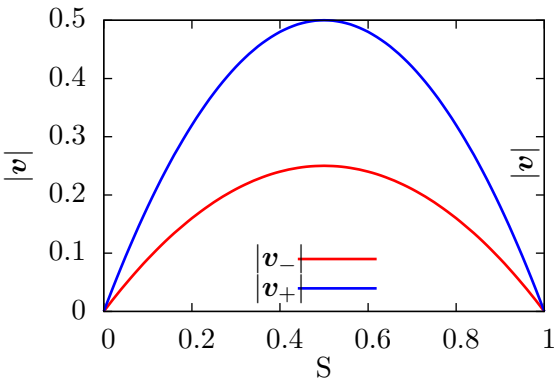

Figure 5: Flux functions at the interface between two rocks with different K

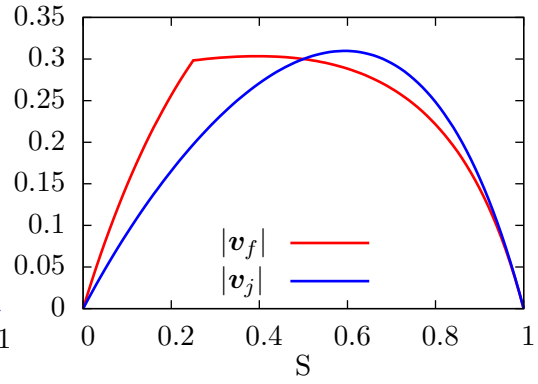

Figure 6: Flux functions at the matrix-fracture interface in the case of different relative permeabilities.

We consider as the initial condition the values

$$S^w(t = t_0) = \begin{cases} 0.8 & \text{if } x < 0 \\ 0.1464 & \text{if } x > 0. \end{cases}$$

We want to solve the problem inserting a slanting fracture $\gamma = \{(x, y) \in \Omega : y = 10x - 9\}$ with the same properties of the surrounding porous medium, *i.e.* $K_f = K_+$ for $y > 0$ and $K_f = K_-$ for $y < 0$, $\Phi_f = \Phi$, the same relative permeabilities and the same initial conditions. The solution should be comparable with the one obtained with the same data without any fractures inside the domain. Results are shown in Figure 10. We compare the solution of a one-dimensional problem with two rock types without fractures in the domain with the solution of the two-dimensional problem in the presence of the fracture. For both problems the time step is selected such that the CFL constant is 1/8. The one dimensional solution, computed on a fine grid, can be regarded as a reference solution since the two dimensional problem is invariant in the x direction. The two results are in good agreement proving the consistence of the reduced model and of the approximation strategy. It can be also observed that, with respect to the solution obtained with the Exact Riemann Solver the use of the Upstream mobility flux produces an unphysical travelling wave for $y > 0$. Since the two flux functions

do not intersect each other according to the theory [1, 18] the entropy solution consists indeed in a rarefaction from $S^w = 0.8$ to $S^w = 0.5$ and a steady discontinuity from 0.5 to the right value.

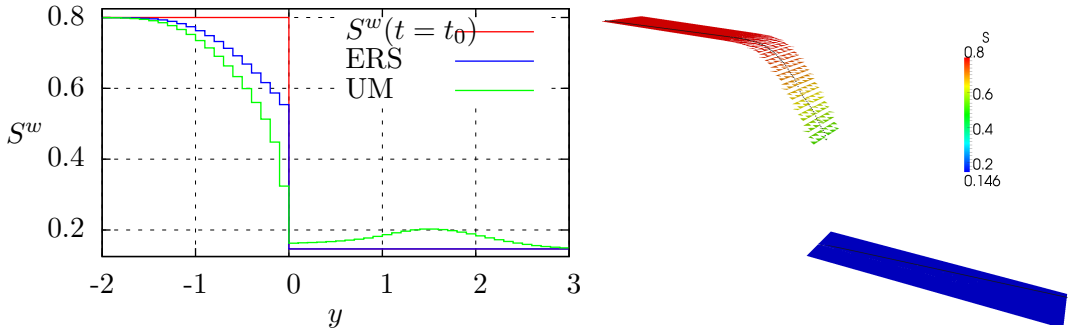

Figure 7: On the left: solution of the 1D problem with mesh size 0.1 with ERS and UM at $t = 1.5$. Right: solution of the corresponding 2D problem with ERS, grids of 880 triangles and 400 segments for the fracture. The black line represents the saturation inside the fracture.

5.2 Numerical flux comparison

We present two example to compare the numerical fluxes UM and ERS in presence of a fracture. Unlike the previous example we consider the fracture as composed by a different rock type with respect to the homogeneous surrounding material.

5.2.1 Example 1

In the first example we impose the same absolute permeability tensor in the porous medium and in the fracture, $\boldsymbol{K}_i = \boldsymbol{I}$ and suppose that the two rock types are characterized by different shapes of the relative permeability functions. We replicate the numerical experiment of [18] selecting

$$k_f^w = S, \quad k_f^n = 1 - S^2, \quad k_j^n = 1 - S^2,$$
$$k_j^w = \begin{cases} 1.75S & \text{if } S \leq 0.25 \\ 0.25S + 0.375 & \text{if } S \geq 0.25 \end{cases}.$$

Here the subscript f denotes the relative permeabilities inside the fracture. The shape of the two flux functions is reported in Figure 6. The other parameters are the same as in the previous example, while the initial condition is $S^w(t = t_0) = 0.5$ in the whole domain. The same value of saturation is imposed on the top (inflow) boundary. The computational domain $\Omega = (0, 1)^2$ is a square cut by a horizontal fracture $\gamma = \{(x, y) \in \Omega : y = 0.525\}$ of thickness $d = 0.01$. We

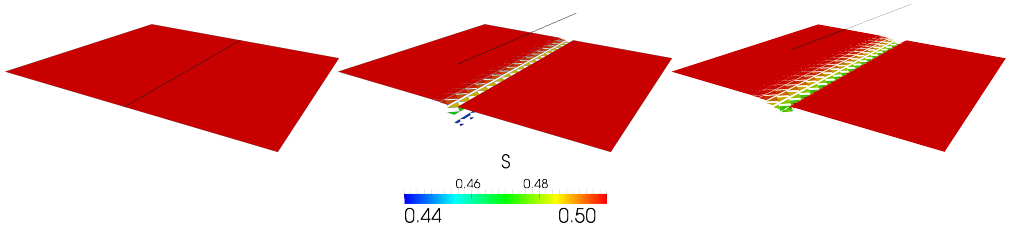

Figure 8: Left: solution obtained with UM, constant for all t. Centre and right: solution with ERS for $t = 0.4$ and $t = 1$, respectively. The black line represents the saturation inside the fracture.

adopt a grid spacing $h = 1/35$ for Ω while $h_f = 1/200$, and the time step is $\Delta t^m \approx 2.6 \cdot 10^{-6}$, for all m, to meet the CFL condition.
The result obtained with UM flux and ERS are reported in Figure 8. It can be observed that the solution given by UM, on the left, is the constant value $S^w(t) = 0.5$ for all $t \in \mathcal{I}_T$. Following [14] this solution is to be considered unphysical since is inconsistent with the entropy definition given in [15]. The solution computed

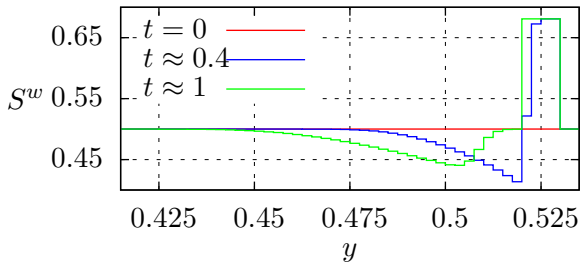

Figure 9: Zoom of the mono-dimensional solution with ERS for two different times, in the fracture ($0.475 < y < 0.575$) and surrounding porous medium.

with the ERS, represented at two distinct time steps, centre and right in Figure 8, evolves in time with a behaviour that is consistent with the analogous experiment in [18]. As the heavier phase flows downwards saturation increases inside the fracture and decreases in the porous medium with a rarefaction. Note that, since the flux is aligned with gravity and the fracture is horizontal no flux occurs along γ. The solution of the 2D problem along any section $x = \overline{x}$ can be compared, since the solution is invariant in the x direction, with a one dimensional problem with a fine grid that is able to capture the fracture. The resulting saturation profile computed with the ERS is reported in Figure 9 for two time steps. The rarefaction wave and the peak of saturation in the fracture are in agreement with the results of the reduced model.

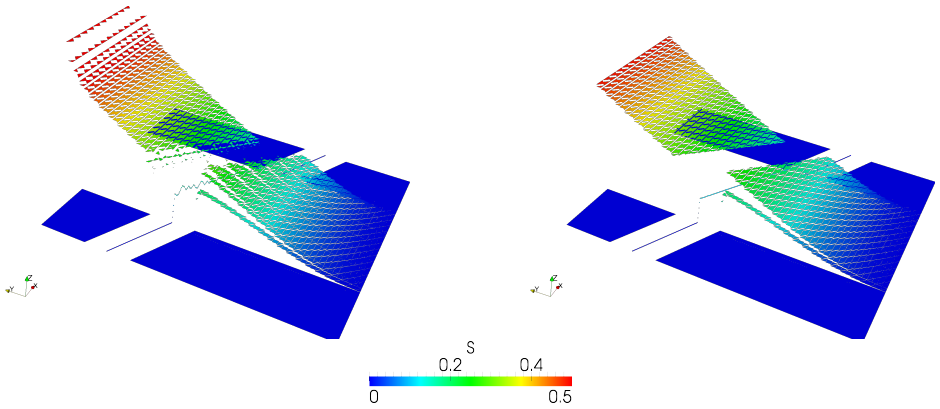

Figure 10: Left: solution obtained with UM, right: solution obtained with ERS. In both cases $t \approx 0.8$.

5.2.2 Example 2

Although it is in principle possible to select different relative permeabilities for the fracture and the porous matrix, the available data allow us, in most realistic situations, to characterize the fracture only with a different value of the absolute permeability. We want to test the behaviour of the method in this particular case for the two different choices of the numerical flux. We will consider the absolute and relative permeabilities introduced in section 5.1 but, this time, assigning the higher absolute permeability to the fracture and the lower to the homogeneous porous matrix, thus

$$\boldsymbol{K}_j = \boldsymbol{I} \quad \text{and} \quad \boldsymbol{K}_f = 2\boldsymbol{I}.$$

The computational domain is the unit square $\Omega = (0,1)^2$, discretized with a grid of about 2500 triangles. The fracture is the line of equation $\gamma = \{(x,y) \in \Omega : \ y = 0.5x - 0.8\}$, discretized with 400 segments. We chose the time step as $\Delta t^m \approx 1.53 \cdot 10^{-6}$, for all m, such that the CFL constant is always lower or equal to $1/8$. We set $S^w = 0$ everywhere as the initial condition and $\overline{S} = 1$ on part of the top boundary, *i.e.* for $y = 0$ and $0.25 < x < 0.75$. As in the previous problems we set $\boldsymbol{u} = 0$ and $\rho^w |\boldsymbol{g}| = 2$, $\rho^n |\boldsymbol{g}| = 1$. Note that, with respect to the previous case, gravity has an effective component in the direction of the fracture therefore we should expect a more complex behaviour when the heavier phase, flowing downwards, interacts with the fracture. The problem is solved numerically with the upstream mobility and with the exact Riemann solver. Figure 10 shows the solution of the problem for both fluxes. The two solutions exhibit a different saturation profile since the UM computes, at the inflow, a different propagation speed from the exact solution of the Riemann problem. The most relevant difference is, however, related to the matrix-fracture interaction. We can see that the solution obtained with the UM exhibits oscillations along the fracture, leading to oscillations also in the surrounding medium, while the solution obtained with the ERS does not

show any oscillation. The oscillatory solution computed by UM is due to a development of a traveling wave inside the fracture, similar to the one observed in section 5.1. The waves are generated at different times since the fracture is not orthogonal to the flux, and interact generating a complex solution inside and outside the fracture. As discussed in the analogous example this behavior is unphysical and suggests that, even in very simple cases, the discontinuity of the flux function could give rise to solutions that do not fulfill the entropy condition if the Riemann problem at the interface is not solved exactly.

5.3 Flow driven by gravity

Let us consider once again a flow driven by gravity, *i.e.* $\boldsymbol{u}_j \equiv \hat{\boldsymbol{u}} \equiv 0$, in a square domain $\Omega = (0,1)^2$ cut by the fracture $\gamma = \{(x,y) \in \Omega : \ y = -2x + 1.4\}$, where we set the initial saturation $S_0 = 0.5$ in the circle $(x-0.45)^2 + (y-0.15)^2 < 0.4^2$. The properties of the fluid and the media are reported in Table 1. In this example we want to reproduce the effect of a conductive fault/fracture on the flow of a buoyant fluid (for instance CO_2) in a porous medium.

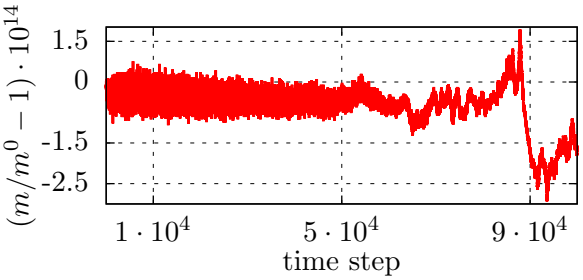

Figure 11: Plot of the conservation of mass over time steps. Here m is the global mass plus the outflow and with m^0 the global mass at initial time.

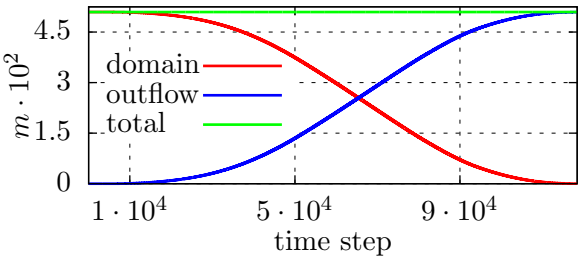

Figure 12: Plot of the conservation of mass over time steps. Here m is the global mass plus the outflow and with m^0 the global mass at initial time.

To this purpose we compare, in Figure 13 the saturation of the non-wetting (light) fluid in two scenarios. In the first case (a) we assign to γ the same permeability of the rest of the medium, neglecting in fact the presence of the fracture, while in the second case (b) we impose to the fracture a permeability

$k_i^n = 1 - S^2$	$k_i^w = S$	$\rho^w = 2$	$\rho^n = 1$
$\boldsymbol{g} = (0, -1)^\top$	$\mu^\alpha = 1$	$\Phi_i = 1$	$\boldsymbol{K}_{1,2} = \boldsymbol{I}$
$d = 0.01$			

Table 1: Fluid and media properties for test case 5.3.

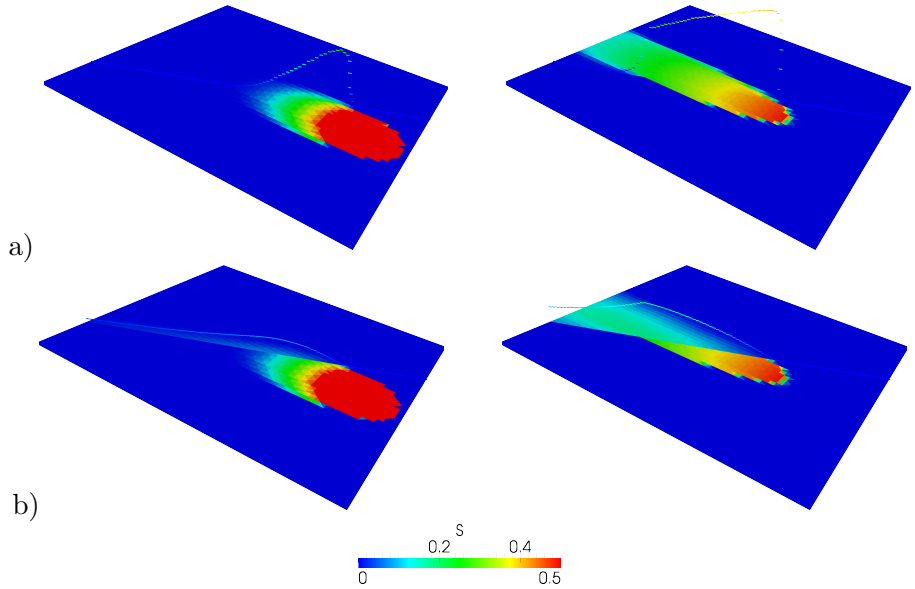

Figure 13: Snapshots of the solution at $t \simeq 1$ in three different cases: on the left S_h without fractures, in the centre S_h and $\hat{S}_h$ with γ whose properties are equal to the bulk medium and on the right with γ more conductive in the tangential direction. Here $\hat{S}_h$ is warped for the sake of visualization.

that is higher in the tangential direction, *i.e.* $K_{f,\boldsymbol{\tau}} = 20$, $K_{f,\boldsymbol{n}} = 1$. We notice that the lighter phase flows upwards due to buoyancy in both cases, but in the case of a conductive fracture the flow inside the fracture is faster, therefore a different saturation pattern is obtained at the outflow boundary. We verified numerically that the method is mass conservative. We represent in Figure 12, for case (b), the amount of the light phase present in the domain at each time step, computed as the integral of ΦS^n in Ω and γ, and the outflow through the top boundary of Ω and γ, to show that the sum remains constant throughout the simulation. For a more quantitative analysis in Figure 11 we represent the mass conservation error computed as the normalized difference between the mass m at each time step, given by the integral inside the domain and the cumulative outflow, and its initial value m_0. The observed oscillations can be regarded as very small compared to the double machine precision indicating that the method is mass conservative.

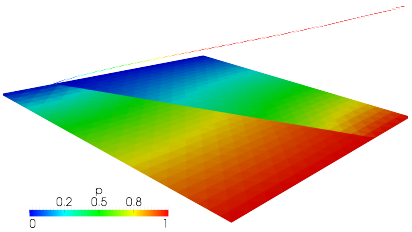

Figure 14: Pressure field, in Ω and γ, at initial time step.

5.4 Fully coupled two-phase flow

In this example we consider the complete coupled two-phase flow model (5) and (6), solved numerically with an IMPES splitting. Let us consider the same domain Ω and fracture γ as in the previous example, but assuming this time that the domain lays in the horizontal plane, thus no gravity effects are present. The flow is driven, in this case, by a pressure gradient resulting from the imposition of $\overline{p} = 1$ at the bottom boundary and $\overline{p} = 0$ at the top, while the left and right boundaries are considered as impermeable. We set as the initial condition $S_0 = 1$ in the circle $(x-0.45)^2+(y-0.15)^2 < 0.4^2$ and consider a fracture that is permeable in the tangential direction and impermeable in the normal direction setting $K_{f,\boldsymbol{\tau}} = 1$ and $K_{f,\boldsymbol{n}} = 10^{-3}$. The remaining properties of the fluids and the media are the same as in the previous test case, see Table 1. The pressure field at $t = 0$ is reported in Figure 14 where the pressure jump, due to the low normal permeability of the fracture, is clearly visible. As a consequence of the impermeable fracture the total velocity field $\boldsymbol{u}$ will be approximately tangent to γ in the region surrounding the fracture. Since the coefficients in (5) depend on saturation the pressure and velocity field will be, in general, different at each time step. Figure 15 compares the evolution of saturation obtained with a constant velocity field, corresponding to $S^n = 0$, with the result of the fully coupled two-phase problem. We notice that even if the solutions look similar in the beginning, the real velocity field changes in time due to the effect of relative permeability and after some time the difference between the two solutions becomes noticeable.

5.5 Two-phase flow through an opening fracture

Finally, we consider the case of a crack that propagates through an heterogeneous domain. The computational domain Ω is crossed by a layer with a very low permeability as sketched in Figure 16. The fracture is represented by the line of equation

$$\gamma = \{(x, y) \in \Omega : \; y = -2x + 1.4, y < 0.55 + 0.1t\},$$

where t denotes a nondimensional time. The propagation of the fracture is imposed a priori and is such that, during the simulation, the crack pierces the

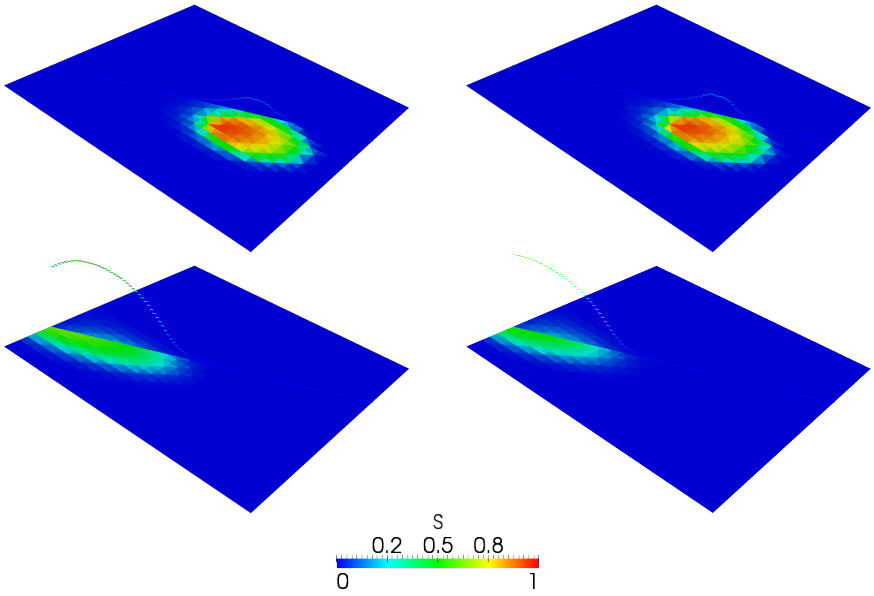

Figure 15: Comparison of S_h and $\hat{S}_h$ for the two strategies: on the left with a constant velocity and on the right the coupled problem. On the top the solution at $t \simeq 0.27$ and on the bottom at $t \simeq 1.1$.

impermeable layer. We consider a fully coupled two-phase flow in the absence of gravity and impose the same initial and boundary conditions as in section 5.4. The permeabilities in the fracture are $K_{f,\boldsymbol{\tau}} = 10$ and $K_{f,\boldsymbol{n}} = 1$, while the permeability in the porous medium is isotropic and set to to 1 everywhere except for the impermeable layer that has $K = 0.01$. The results are shown in Figure 17 at four different times. At $t = 0$ the global pressure exhibits a steep gradient in the impermeable layer, which is not entirely cut by the fracture yet. As the light phase starts to flow upwards it enters the fracture and flows preferably along it thanks to the high tangential permeability. Finally, once the fracture has propagated through the whole thickness of the impermeable layer, the light

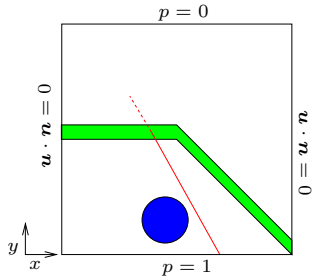

Figure 16: Domain crossed by a low-permeability layer cut by an opening fracture. The initial saturation is indicated by the blue circle.

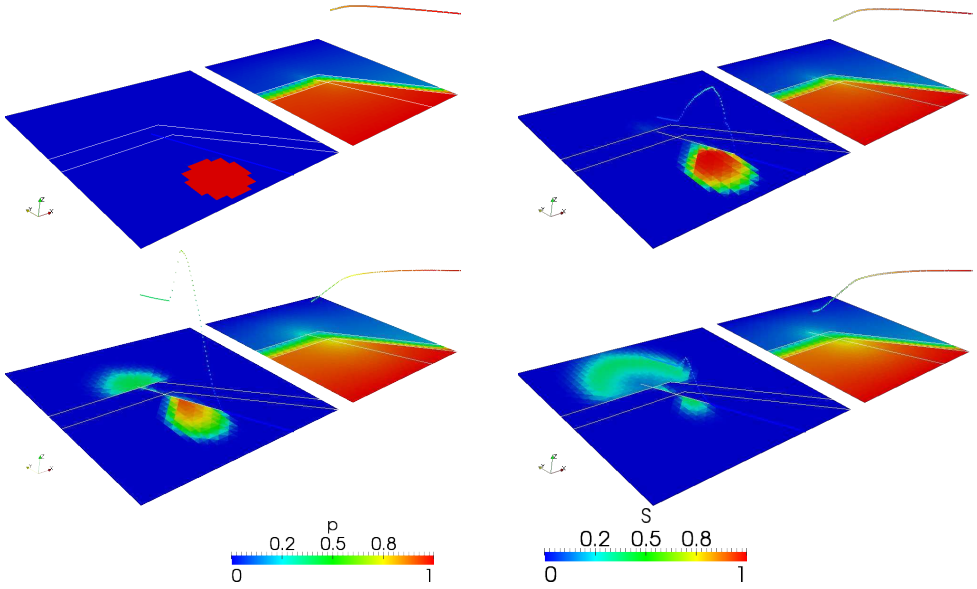

Figure 17: Wetting phase saturation (bottom left) and global pressure (top right) at four different times. The fractures propagates with an imposed time law cutting the impermeable layer.

phase can flow in the top part of the domain through the fracture. At the same time, a local drop of the global pressure can be observed in the bottom part of the domain.

6 Conclusions

In this paper we have proposed an original method for the numerical simulation of two-phase flows in fractured porous media, in the framework of reduced models. In particular we extended the method introduced in [7] for the simulation of single phase Darcy flows with the XFEM to the two-phase case introducing an additional equation for the saturation. An IMPES sequential splitting was used to decouple the two problems. The reduced problem for the saturation inside the fracture, and the coupling conditions between the fracture and the porous matrix were derived following [13] in the limit of negligible capillary pressure. As concerns the numerical approximation, the same non-conforming grid was used for the Darcy and the saturation problem, which was solved with the finite volume method accounting for cut cells and matrix-fracture exchanges. We have shown with numerical experiments that the results of the reduced model are consistent with those of the original problem solved on a very fine grid that is able to resolve the fracture. Moreover, we have shown that the method is mass conservative. A comparison between the Godunov flux and the Upstream Mobility flux revealed that, even in simple cases, the latter can give inaccurate or

even unphysical solution in the presence of a discontinuous flux function. Since the porous matrix and the fracture are typically characterized by different permeabilities the flux function is in general discontinuous at the matrix-fracture interface in the problems of our interest, thus, the choice of a suitable numerical flux is a critical issue. The method has been applied to synthetic test cases with qualitatively correct results. Of particular interest for the problem of CO_2 sequestration is the simulation of CO_2 leakage through a propagating crack. In this work we have considered an imposed evolution of the fractures, however, thanks to the use of XFEM the method could be in the future coupled with a suitable solver for the mechanics of the rock to predict the propagation of fractures in the presence of overpressure.
Future work will focus on the extension of the method to realistic geometries and values of the parameters. Moreover, capillary effects should be included in the saturation equation. In an operator splitting framework this can be achieved adding a diffusive step after the solution of the hyperbolic equation. Finally, we point out that the CFL condition can represent a severe constraint for our solution strategy even if the mesh is not refined to resolve the fractures. Indeed, being the grid non conforming with the fracture small cut cells can form for some configuration and limit the maximum time step size. Suitable numerical techniques to overcome this limitation will be the subject of future study in the view of more realistic and computationally demanding test cases.

7 Acknowledgments

This work has been partially supported by ENI s.p.a. The second author also acknowledges the support of MIUR through the PRIN09 project n. 2009Y4RC3B 001. The authors wish to thank Luca Formaggia, Jérôme Jaffré and Jean Roberts for many fruitful discussions.

References

[1] Adimurthi, Jérôme Jaffré, and G. D. Veerappa Gowda. Godunov-type methods for conservation laws with a flux function discontinuous in space. *SIAM J. Numer. Anal.*, 42(1):179–208 (electronic), 2004.

[2] Clarisse Alboin, Jérôme Jaffré, Jean E. Roberts, Xuewen Wang, and Christophe Serres. *Domain decomposition for some transmission problems in flow in porous media*, volume 552 of *Lecture Notes in Phys.*, pages 22–34. Springer, Berlin, 2000.

[3] Philippe Angot, Franck Boyer, and Florence Hubert. Asymptotic and numerical modelling of flows in fractured porous media. *M2AN Math. Model. Numer. Anal.*, 43(2):239–275, 2009.

[4] Jacob Bear. *Dynamics of Fluids in Porous Media*. American Elsevier, 1972.

[5] G. Chavent, G. Cohen, and J. Jaffré. A finite element simulator for incompressible two-phase flow. *Transport in porous media*, 2:465–478, 1987.

[6] Guy Chavent and Jérôme Jaffré. *Mathematical Models and Finite Elements for Reservoir Simulation*, volume 17. Elsevier, 1986.

[7] Carlo D'Angelo and Anna Scotti. A Mixed Finite Element Method for Darcy Flow in Fractured Porous Media with Non-Matching Grids. *Mathematical Modelling and Numerical Analysis*, 2011.

[8] Alessio Fumagalli. *Numerical Modelling of Flows in Fractured Porous Media by the XFEM Method*. PhD thesis, Politecnico di Milano, 2012.

[9] Alessio Fumagalli and Anna Scotti. Numerical modelling of multiphase subsurface flow in the presence of fractures. *Communications in Applied and Industrial Mathematics*, December 2011.

[10] Alessio Fumagalli and Anna Scotti. A reduced model for flow and transport in fractured porous media with non-matching grids. Technical Report 03/2012, Politecnico di Milano, January 2012.

[11] S. Godunov. Finite difference methods for numerical computation of discontinuous solutions of the equations of fluid dynamics. *Math.Sbornik*, 47:271–306, 1959.

[12] Anita Hansbo and Peter Hansbo. An unfitted finite element method, based on Nitsche's method, for elliptic interface problems. *Comput. Methods Appl. Mech. Engrg.*, 191(47-48):5537–5552, 2002.

[13] Jérôme Jaffré, M. Mnejja, and J.E. Roberts. A discrete fracture model for two-phase flow with matrix-fracture interaction. *Procedia Computer Science*, 4:967–973, 2011.

[14] E. F. Kaasschieter. Solving the Buckley-Leverett equation with gravity in a heterogeneous porous medium. *Comput. Geosci.*, 3(1):23–48, 1999.

[15] K. H. Karlsen, N. H. Risebro, and J. D. Towers. L^1 stability for entropy solutions of nonlinear degenerate parabolic convection-diffusion equations with discontinuous coefficients. *Skr. K. Nor. Vidensk. Selsk.*, (3):1–49, 2003.

[16] C. W. MacMinn, M. L. Szulczewski, and R. Juanes. CO_2 migration in saline aquifers. Part 1. Capillary trapping under slope and groundwater flow. *J. Fluid Mech.*, 662:329–351, 2010.

[17] Vincent Martin, Jérôme Jaffré, and Jean E. Roberts. Modeling fractures and barriers as interfaces for flow in porous media. *SIAM J. Sci. Comput.*, 26(5):1667–1691, 2005.

[18] Siddhartha Mishra and Jérôme Jaffré. On the upstream mobility scheme for two-phase flow in porous media. *Comput. Geosci.*, 14(1):105–124, 2010.

MOX Technical Reports, last issues

Dipartimento di Matematica "F. Brioschi",
Politecnico di Milano, Via Bonardi 9 - 20133 Milano (Italy)

44/2012 Fumagalli, A.; Scotti, A.
A numerical method for two-phase flow in fractured porous media with non-matching grids

43/2012 Secchi, P.; Vantini, S.; Vitelli, V.
A Case Study on Spatially Dependent Functional Data: the Analysis of Mobile Network Data for the Metropolitan Area of Milan

42/2012 Lassila, T.; Manzoni, A.; Quarteroni, A.; Rozza, G.
Generalized reduced basis methods and n width estimates for the approximation of the solution manifold of parametric PDEs

41/2012 Chen, P.; Quarteroni, A.; Rozza, G.
Comparison between reduced basis and stochastic collocation methods for elliptic problems

40/2012 Lombardi, M.; Parolini, N.; Quarteroni, A.
Radial basis functions for inter-grid interpolation and mesh motion in FSI problems

39/2012 Ieva, F.; Paganoni, A.M.; Ziller, S.
Operational risk management: a statistical perspective

38/2012 Antonietti, P.F.; Bigoni, N.; Verani, M.
Mimetic finite difference approximation of quasilinear elliptic problems

37/2012 Nobile, F.; Pozzoli, M.; Vergara, C.
Exact and inexact partitioned algorithms for fluid-structure interaction problems with finite elasticity in haemodynamics

36/2012 Canuto, C.; Verani, M.
On the Numerical Analysis of Adaptive Spectral/hp Methods for Elliptic Problems

35/2012 Pigoli, D.; Aston, J.A.D.; Dryden, I.L.; Secchi, P.
Distances and Inference for Covariance Functions